We are IntechOpen, the world's leading publisher of Open Access books Built by scientists, for scientists

6,900
Open access books available

185,000
International authors and editors

200M
Downloads

Our authors are among the

154
Countries delivered to

TOP 1%
most cited scientists

12.2%
Contributors from top 500 universities



WEB OF SCIENCE™

Selection of our books indexed in the Book Citation Index in Web of Science™ Core Collection (BKCI)

Interested in publishing with us?
Contact book.department@intechopen.com

Numbers displayed above are based on latest data collected.
For more information visit www.intechopen.com



4

Collective Plasmonic States Emerged in Metallic Nanorod Array and Their Application

Masanobu Iwanaga
National Institute for Materials Science and
Japan Science and Technology Agency (JST), PRESTO
Japan

1. Introduction

Plasmons are well known as collective excitations of free electrons in solids. Simple unit structures are nanoparticles such as spheres, triangles, and rods. Optical properties of metallic nanoparticles were reported at the beginning of the 20th century (Maxwell-Garnett, 1904, 1906). Now it is well known that the resonances in metallic nanoparticles are described by Mie theory (Born & Wolf, 1999). It is interesting to note that the studies on nanoparticles were concentrated at the beginning of the century, at which quantum mechanics did not exist. Shapes and dimensions of metallic nanoparticles such as triangles and rods were clearly classified by their dark-field images after a century from the initial studies on nanoparticles (Kuwata et al., 2003; Murray & Barnes, 2007). Nanoparticles were revived around 2000 in the era of nanotechnology.

It may be first inferred that dimers and aggregations of metallic nanostructures have bonding and anti-bonding states stemming from Mie resonances in the nanoparticles. The conjecture was confirmed in many experimental studies (For example, Prodan et al., 2003; Liu et al., 2007; Liu et al., 2009). Dimer structures composed of a pair of nanospheres or nanocylinders are one of the most examined structures. At the initial stage of the dimer study, very high-enhancement of electric field at the gap was frequently reported based on a computational method of finite-difference time domain (FDTD), which is directly coded from classical electromagnetics or Maxwell equations. However, recent computations including nonlocal response of metal, which is quantum mechanical effect, disagree the very high-enhancement (García de Abajo, 2008; McMahon et al., 2010). Especially, as the gap is less than 5 nm, the discrepancies in cross section and extinction becomes prominent. While the physics in dimensions of nm and less obeys quantum mechanics in principal, many experimental and theoretical results show that classical electromagnetics holds quite well even in tens of nm scale. Thus, it is not yet conclusive where the boundary of classical electromagnetics and quantum mechanics exists in nm-scale plasmonics. It will be elucidated when further development of nanofabrication techniques will be able to produce nm-precision metallic structures with reliable reproducibility. Taking the present status of nanotechnology into account, we focus on structures, such as gap, of the dimension more than 5 nm, where classical electromagnetics holds well.

Contemporary nanofabrication technology can produce a wide variety of plasmonic structures, which are usually made of metals. In addition to unit structures such as

nanoparticles, periodic structures are also produced, where surface plasmon polaritons (SPPs) are key resonances. Strictly, the SPPs in periodic structures are different from the original SPPs induced at ideally flat metal-dielectric interface. Periodic structures enable to reduce the original SPP into the first Brillouin zone; it is therefore reasonable to call the SPPs in periodic structures reduced SPPs. The reduced SPPs were known since 1970s (Raether, 1988) and were revived as a type of resonances yielding extraordinary transmission in a perforated metallic film (Ebbesen et al., 1998).

When producing periodic array of nanoparticles, what is expected? Periodic structures are aggregation of monomers and dimers, and have photonic band structures. By structural control, it is expected to obtain desired photonic bands, for example, wave-number-independent, frequency-broad band, which is not obtained in dimers and so on. In terms of photovoltaic applications, light absorbers working at a wide energy and incident-angle (or wave-number) ranges are preferred. On the other hand, if one access highly enhanced electromagnetic fields, states of high quality factor, which are associated with narrow band, may be expected. Thus, the designs of plasmonic structures vary in accordance with needs. Main purpose of this chapter is to show some of concrete designs of plasmonic structures exhibiting collective oscillations of plasmons and broad-band plasmonic states, based on realistic and precise computations.

This chapter consists of 7 sections. Computational methods are described in section 2. One-dimensional (1D) and two-dimensional (2D) plasmonic structures are examined based on numerical results in sections 3 and 4, respectively. As for applications, light absorption management is examined in section 3 and polarization manipulators of subwavelength thickness are shown in section 4. Conclusion is given in section 5.

2. Computational methods

Before describing the results of 1D and 2D plasmonic structures, computational methods are noted in this section. In section 2.1, Fourier modal method or rigorously coupled-wave approximation (RCWA) is described, suitable to compute linear optical spectra such as reflection and transmission. In section 2.2, finite element method is explained, which is employed to evaluate electromagnetic field distributions. Although the two methods have been already established, the details in implementation are useful when researchers unfamiliar to plasmonics launch numerical study. Furthermore, the detailed settings are described.

Realistic simulations are intended here. As material parameters, constructive equations in Maxwell equations for homogeneous media have permittivity and permeability (Jackson, 1999). In the following computations, we took permittivity of metals from the literature compiling measured data (Rakić et al., 1998). The permittivity of transparent dielectric was set to be typical values: that of air is 1.00054 and that of SiO_2 is 2.1316. The permittivity of Si was also taken from literature (Palik, 1991). At optical wavelengths, it is widely believed that permeability is unity in solids (Landau et al., 1982); to date, any exception has not been found in solid materials.[1]

[1] Metamaterials were initially intended to realize materials of arbitrary permittivity and permeability by artificial subwavelength structures (Pendry & Smith, 2004). This strategy has been successful especially at microwaves.

2.1 Optical spectra

Linear optical responses from periodic structures are observed as reflection, transmission and diffraction. To calculate the linear optical responses, it is suitable to transform Maxwell equations into the Fourier representation. By conducting the transformation, the equation to be solved is expressed in the frequency domain; therefore, optical spectra are obtained in the computation with varying wavelength. In actual computations, it is crucial to incorporate algorithm which realizes fast convergence of the Fourier expansion. If one does not adopt it, Fourier expansion shows extremely slow convergence and practically one cannot reach the answer. The algorithm could not be found for a few decades in spite of many trials. The issue was finally resolved for 1D periodic systems in 1996 (Lalanne & Morris, 1996; Li, 1996b; Granet & Guizal, 1996) and succeedingly for 2D periodic systems in 1997 (Li, 1997). The Fourier-based method is often called RCWA. Commercial RCWA packages are now available. In this study, we prepared the code by ourselves incorporating the Fourier factorization rule (Li, 1997) and optimized it for the vector-oriented supercomputers.

In general, the periodic structures are not single-layered but are composed of stacked layers. Eigen modes in each layer expressed by Fourier-coefficient vectors are connected at the interfaces by matrix multiplication. The intuitive expression results in to derive transfer matrix (Markoš, 2008). Practically, transfer matrix method is not useful because it includes exponentially growing factors. To eliminate the ill-behaviour, scattering matrix method is employed. Transfer and scattering matrices are mathematically equivalent. In fact, scattering matrix was derived from transfer matrix by recurrent formula (Ko & Inkson, 1988; Li, 1996a). The derivations were independently conceived for different aims: the former was to solve electronic transport in quantum wells of semiconductors as an issue in quantum mechanics (Ko & Inkson, 1988) and the latter was to calculate light propagation in periodic media as an issue in classical electromagnetics (Li, 1996a).

In actual implementation, truncations of Fourier expansions are always inevitable as written in equation (1), which shows Lth-order truncation. Of course, the Fourier expansion is exact as $L\rightarrow\infty$.

$$E(x,y)=\sum_{m,n=0,\pm1,\pm2,\cdots,\pm L}E_{mn}\exp(ik_x x+ik_y y+2\pi im/d_x+2\pi in/d_y) \quad (1)$$

In equation (1), 2D periodic structure of the periodicities of d_x and d_y is assumed and incident wave vector has the components k_x and k_y. The term E_{mn} is Fourier coefficient of function $E(x, y)$. For 2D periodic structures shown later, the truncation order is set to be L= 20. Then, estimated numerical fluctuations were about 1%. For 1D periodic structures, one can assume that d_y is infinity in equation (1); as a result, requirements in numerical implementation become much less than 2D cases. It is therefore possible to set large order such as L=200 and to suppress numerical fluctuations less than 0.5%.

Optical spectra calculated numerically by the Fourier modal method were compared with measured spectra; good agreement was confirmed in stacked complementary 2D plasmonic crystal slabs, which have elaborate depth profiles (Iwanaga, 2010b, 2010d).

2.2 Electromagnetic-field distributions

Electromagnetic-field distributions were computed by employing finite element method (COMSOL Multiphysics, version 4.2). One of the features is to be able to divide constituents by grids of arbitrary dimensions.

To keep precision at a good level, transparent media were divided into the dimensions less than 1/30 effective wavelength. As for metals, much finer grids are needed. Skin depth of metals at optical wavelengths is a few tens of nm; therefore, grids of sides of a few nm or less were set in this study. Such fine grids result in the increase in required memory in implementation. Even for the unit domain in 2D periodic structures, which is minimum domain and becomes three-dimensional (3D) as shown in Fig. 7, the allocated memory easily exceeded 100 GB. As for 1D structures, the unit domain is 2D and requires much less memory in implementation. Accordingly, computation time is much shorter; in case of Fig. 3, it took about ten seconds to complete the simulation.

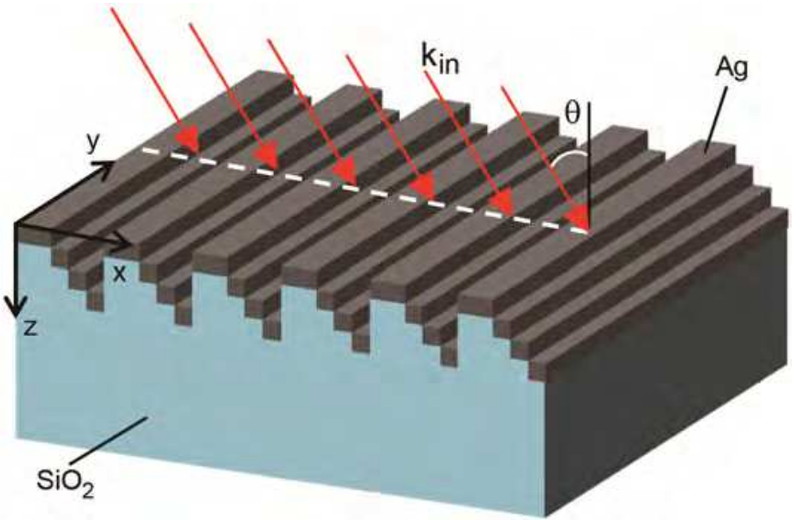


Fig. 1. Schematic drawing of an efficient 1D plasmonic light absorber of Ag nanorod array on SiO_2 substrate, which was found based on the search using genetic algorithm. Plane of incidence is set to be parallel to the *xz* plane.

The finite element method was applied for resolving the resonant states in the stacked complementary 2D plasmonic crystal slabs and revealed the eigen modes successfully (Iwanaga, 2010c, 2010d).

3. 1D periodic metallic nanorod array

Light absorbers of broad band both in energy and incident-angle ranges were numerically found (Iwanaga, 2009) by employing simple genetic algorithm (Goldberg, 1989). One of the efficient absorbers is a 1D metallic nanorod array as drawn in Fig. 1. The Ag nanorods (dark grey) are assumed to be placed on the step-like structure of SiO_2 (pale blue). Periodic direction was set to be parallel to the *x* axis, and the periodicity is 250 nm. The nanorods are parallel to the *y* axis and infinitely long. The nanorods in the top layer have the *xz* rectangular sections of 100×50 nm². The other nanorods have the *xz* square sections of 50×50 nm².

In 1D structures, it was found that depth profiles are crucial to achieve desired optical properties. Single-layered 1D structures have little degree of freedom to meet a designated optical property whereas 1D structures of stacked three layers have enough potentials to reach a given goal (Iwanaga, 2009).

In this section, we clarify the light-trapping mechanism by examining the optical and absorption properties, and electromagnetic field distributions. Collective electrodynamics between the nanorods plays a key role to realize the doubly broad-band absorber.

3.1 Optical responses and light absorption

Incident plane waves travel in the *xz* plane (that is, the wave vectors $\mathbf{k}_{in}$ are in the *xz* plane) as shown in Fig. 1, keeping the polarization to be *p* polarization, that is, incident electric-field vector $\mathbf{E}_{in}$ is in the *xz* plane. To excite plasmonic states in 1D periodic systems, the *p* polarization is essential. If one illuminates the 1D object by using *s*-polarized light (that is, $\mathbf{E}_{in}$ parallel to *y*), plasmonic states stemming from SPPs are not excited. Absorbance spectra under *p* polarization at incident angles θ of -40, 0, and 40 degrees are shown in Fig. 2(a) with solid line, dashed line, and crosses, respectively. The sign of incident angles θ is defined by the sign of *x*-component $k_{in,x}(=|\mathbf{k}_{in}|\sin\theta)$ of incident wave vector. Absorbance *A* in % is defined by

$$A = 100 - \sum_{n=0,\pm1,\pm2,\ldots}(R_n + T_n) \tag{2}$$

where R_n and T_n are *n*th-order reflective and transmissive diffractions, respectively. R_0 denotes reflectance and T_0 stands for transmittance. We computed linear optical responses R_n and T_n by the Fourier modal method described in section 2.1, and evaluated *A* by use of equation (2). The symbols R_0 and T_0 are respectively expressed simply as *R* and *T* from now on. In the 1D structure in Fig. 1, since the periodicity is 250 nm, T_n and R_n for $n \neq 0$ are zero for θ = 0° in Fig. 2(a) and zero for θ = -40° at more than 525 nm.

In Fig. 2(a), absorption significantly increases at θ = -40° in the wavelength range longer than 600 nm. It is to be stressed that absorption is more than 75% in a wide range from 600 to 1000 nm. Thus, the 1D structure in Fig. 1 works as a broad-band absorber in wavelengths from the visible to near-infrared ranges.

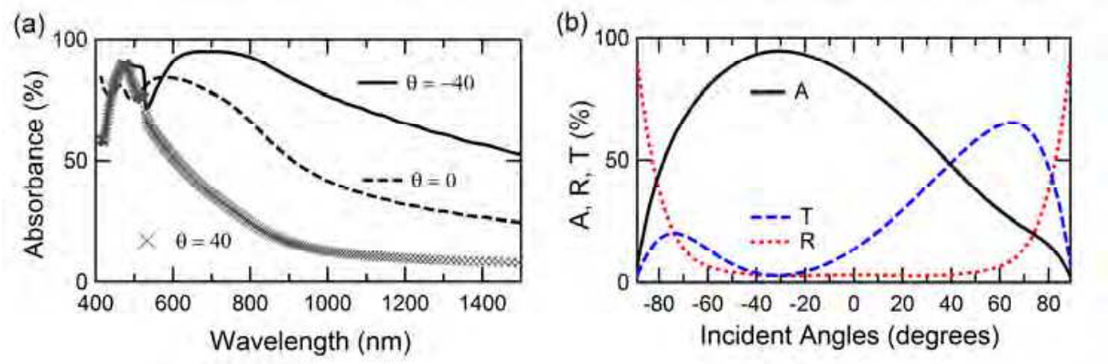


Fig. 2. (a) Absorption spectra at -40° (solid line), 0° (dashed line), and 40° (crosses) under *p* polarization. (b) Spectra of *A* (solid line), *R* (dotted line), and *T* (dashed line) at 620 nm dependent on incident angles.

In Fig. 2(b), The *A* spectrum at 620 nm dependent on incident angles is shown with solid line. The corresponding *T* and *R* spectra are shown with blue dashed and red dotted lines, respectively. Note that diffraction does not appear at this wavelength.

The *T* spectrum in Fig. 2(b) exhibits asymmetric distribution for incident angles θ, indicating that the structure in Fig. 1 is optically deeply asymmetric. In contrast, the *R* spectrum is symmetric for θ and the relation of $R(\theta)=R(-\theta)$ is satisfied; the property is independent of structural symmetry and is known as reciprocity (Potten, 2004; Iwanaga et al., 2007b). The *A* spectrum takes more than 80% at a wide incident-angle range from 5° to -60°. It is thus shown that the 1D periodic structure in Fig. 1 is a doubly broad-band light absorber.

3.2 Magnetic-field and power-flow distributions

To reveal the plasmonic state inducing the doubly broad-band absorption in Fig. 2, we examine here the electromagnetic field distributions at 620 nm and θ = -40°, evaluated by the finite element method. As described in section 3.1, incident plane waves are *p*-polarized and induce transverse magnetic (TM) modes in the 1D periodic structure. Therefore, magnetic-field distribution is suitable to examine the features of the plasmonic state.

In Fig. 3(a), magnetic-field distribution is presented; the magnetic field has only *y* component under *p* polarization and the *y*-component of magnetic field is shown with colour plot. Figure 3(a) shows a snapshot of the magnetic field, where the phase is defined by setting incident electric field $\mathbf{E}_{in}=(\sin(-40°), 0, \cos(-40°))$ at the left-top corner position. The propagation direction of incidence is indicated by arrows representing incident wave vectors $\mathbf{k}_{in}$. To show a wide view at the oblique incidence, the domain in the computation was set to include five unit cells. We assigned the *yz* boundaries (that is, the left and right edges) periodic boundary condition.

The magnetic field distribution in Fig. 3(a) forms spatially oscillating pairs indicated by the signs + and -. It is to be noted that the oscillating pairs are larger than each metallic nanorod and are supported by three or four nanorods. The distributions are enhanced at the vicinity of nanorod array and strongly suggest that collective oscillations take place, resulting in the broad absorption band. As for plasmonic states, resonant oscillations inside metallic nanorod have been observed in most cases, which are attributed to Mie-type resonances (Born & Wolf, 1999). The present resonance is distinct from Mie resonances and has not been found to our best knowledge.

In Fig. 3(b), time-averaged electromagnetic power-flow distribution is shown. The power flow is equivalent to Poynting flux at each point. The *z*-component of the power flow is shown with colour plot and the vectors of power flow are designated by arrows, which are shown in the logarithmic scale for clarity. Oblique incidence is seen at the top of the panel and the power flow successfully turns around the nanorods, going into SiO_2 substrate. In addition to this finding, let us remind that the sum of *R* and *T* are at most 10% as shown in Fig. 2(b), that the power flow in the substrate is not far-field component but mostly evanescent components, and that most of incident power is consumed at the vicinity of the nanorod array. Therefore, incident radiation is considered to be effectively trapped at the vicinity of the nanorod array, especially in the substrate. Management of electromagnetic power flow is a key to realize photovoltaic devices of high efficiency.

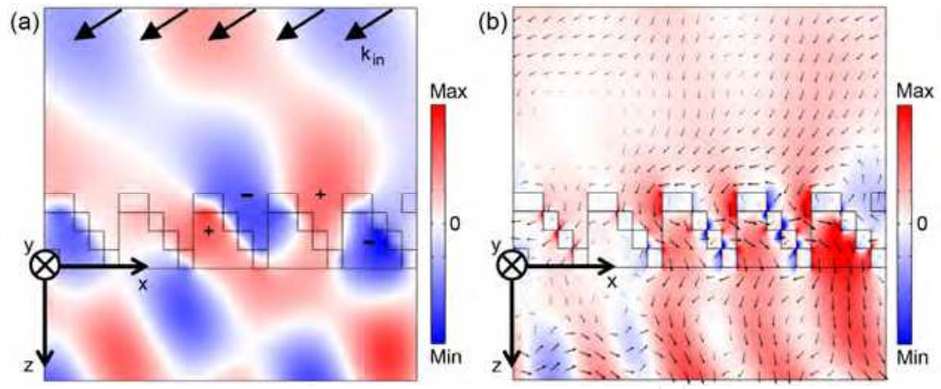


Fig. 3. (a) A snapshot of *y*-component of magnetic field (colour plot). Incident wave vectors are shown with arrows on the top. (b) Time-averaged electromagnetic power flow of *z* component (colour plot). Vectors (arrows) are represented in the logarithmic scale.

3.3 Management of incident light for photovoltaic applications

As is shown in sections 3.1 and 3.2, periodic structure of metallic nanorod array can be broad-band light absorber concerning both wavelengths and incident angles. Good light absorbers are preferred to realize more efficient photovoltaic devices. Possibility for the application is discussed here.

In considering producing efficient photovoltaic devices, it is crucial to exploit incident light fully. In the context, perfect light absorbers are usually preferred. However, light absorption and management of light have to be discriminated. If plasmonic absorbers consume incident light by the resonances resident inside metallic nanostructures such as Mie resonance, photovoltaic parts cannot use the incident light. Thus, it is not appropriate to optimize light absorption by metallic nanostructures when one tries to incorporate them into photovoltaic devices. Instead, one should manage to convert incident light to desired distributions by metallic nanostructures (Catchpole & Polman, 2008a, 2008b). In Fig. 3(b), we have shown that incident light effectively travels into substrate, in which photovoltaic parts will be made. Additionally, most of the light taken in is converted to enhanced evanescent waves. In comparison with the incident power, the power of the evanescent wave is more than a-few-fold enhanced. Such local enhancement of electromagnetic fields is preferable in photovoltaic applications.

As is widely known, management of incident light has been conducted in Si-based solar cells. At the surface, textured structures are usually introduced to increase the take-in amount of light (Bagnall & Boreland, 2008). The difference between the textured structures and the designed metallic nanostructures exists in the enhancement mechanism; the former has no enhancement while the latter can have local resonant enhancement as described above.

In actual fabrications of photovoltaic devices incorporating metallic nanostructures, plasmonic structures will be made on semiconductors. The structure in Fig. 1 is made on SiO_2 and has to be redesigned because the permittivity of SiO_2 and semiconductor such as Si is quite different at the visible range. In this section, we have shown actual potentials of plasmonic structures for light management through a concrete 1D periodic structure of nanorod array. Since genetic algorithm search is robust and applicable to issues one wants

to find solutions (Goldberg, 1989), we positively think of finding plasmonic structures for photovoltaic applications.

In further search, 2D structures will be the targets, independent of incident polarizations. As for the actual fabrications, one may think that the step-like structure as shown in Fig. 1 are hard to produce by current top-down nanofabrication technique. In fact, there is hardly report that 90° etching is successfully executed. However, there is enough room to improve fabrication procedures; for example, if one could prepare hard mask and use calibrated aligner to conduct dry etching of semiconductors, it would be possible to etch down at almost 90° and even to produce step-like structures.

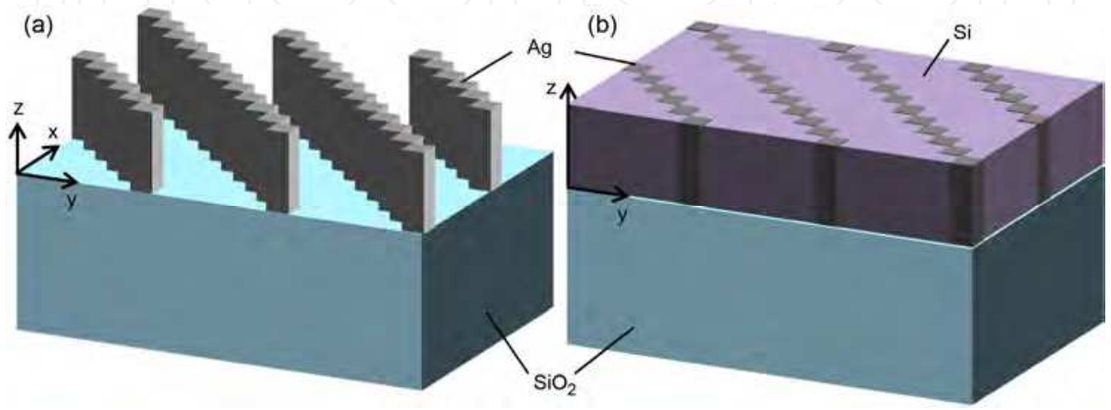


Fig. 4. Schematic drawing of 2D periodic Ag nanorod arrays on SiO_2 substrate. (a) Free standing in air. (b) Embedded in a Si layer.

4. 2D periodic metallic nanorod array

2D periodic nanorod array has much variety in design. In this section, we show how modification of unit cell drastically changes the optical properties. As concrete structures, we present the results on the rectangular nanorod array as shown in Fig. 4 and refer to those on circular nanorod array. In addition, it is shown that well-adjusted 2D nanorod arrays work as efficient polarizers of subwavelength thickness. As the application, circular dichroic devices are presented, which include 2D nanorod array as a component.

Before describing the numerical results on 2D metallic nanorod arrays, we mention how they can be fabricated. It is probably easier to produce the structure in Fig. 4(b) than that in Fig. 4(a). Since thin Si wafers can be fabricated in nm-precision as Si photonic crystal slabs are made (Akahane et al., 2003), the procedure of electron-beam patterning, development, metal deposition, and removal of resist results in the structure in Fig. 4(b) Free-standing metallic nanorods seem to be relatively hard to produce. Simple procedure described as for Fig. 4(b) is unlikely to be successful. Instead, other procedures have to be conceived. One of the ways is to modify the fabrication procedure to produce metallic nanopillars of about 300 nm height (Kubo & Fujikawa, 2011).

4.1 Optical properties

In Fig. 5, *T* and *R* spectra of free-standing Ag nanorod arrays are shown. Unit cell structures in the *xy* plane are drawn at the left-hand side. The periodicity is 250, 275, and 240 nm along

both x and y axes in Figs. 5(a), 5(b), and 5(c), respectively. Grey denotes the xy section of Ag nanorods, which is 50×50 nm² in the xy plane. The height of the nanorods was set to be 340 nm. The gaps between nanorods were set to be 0, 5, and 10 nm along the x and y axes in Figs. 5(a), 5(b), and 5(c), respectively.

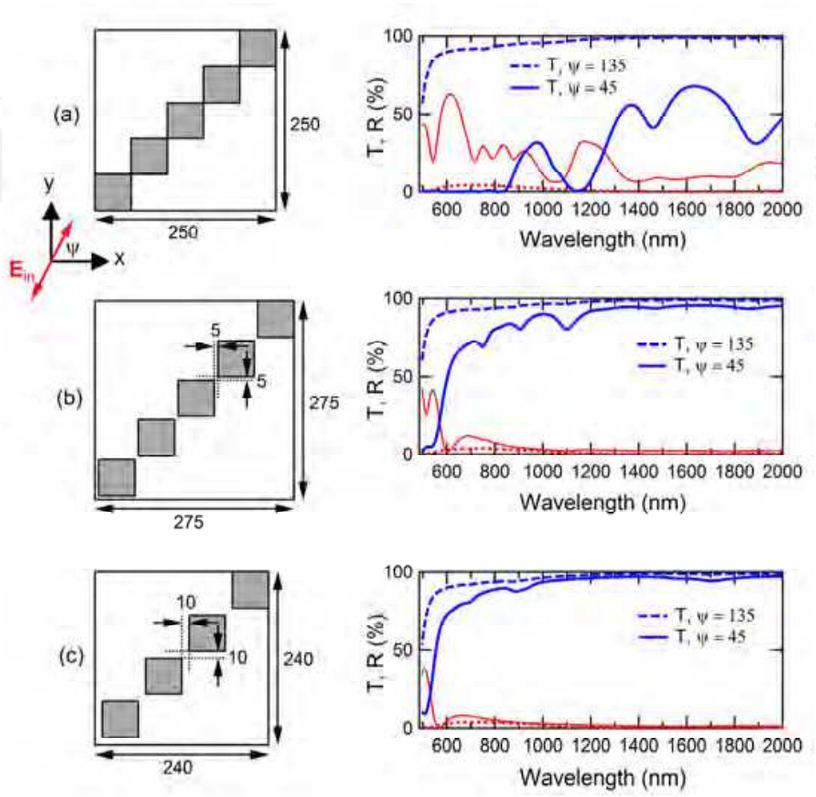


Fig. 5. Unit cell structures and the optical spectra of free-standing Ag nanorod array on SiO_2 substrate. Grey denotes Ag nanorod of 50×50 nm² in the xy plane. Gaps between each nanorod are set along the x and y axes: (a) 0 nm, (b) 5 nm, and (c) 10 nm. Dimensions are written in units of nm. T and R spectra at ψ = 45° are shown with solid and thin lines, respectively. T and R spectra at ψ = 135° are represented with dashed and dotted lines, respectively.

Incident plane waves illuminate the 2D structures at normal incidence. Incident polarization $\mathbf{E}_{in}$ was set to be linear, defined by azimuth angle ψ, that is, the angle between the x axis and the $\mathbf{E}_{in}$ vector, as drawn in Fig. 5(a). In accordance with the symmetry of the unit cell, two polarizations ψ = 45° and 135° were probed. T and R spectra at ψ = 45° are displayed with blue solid and red thin lines, respectively. T and R spectra at ψ = 135° are shown with blue dashed and red dotted lines, respectively.

T spectra at ψ = 45° are sensitive to the gaps. In Fig. 5(a), at the visible range of wavelength less than 800 nm, definite contrast of T at ψ = 45° and 135° is observed. As gaps becomes larger, the contrast of T rapidly diminishes. Actually, in Fig. 5(c) where the gap is 10 nm, T spectra at ψ = 45° and 135° become quite similar in spectral shapes and lose the difference seen in Fig. 5(a). The gap dependence of T spectra implies that there exists resonant state in

the structure of Fig. 5(a) at ψ = 45° and less than 800 nm and that the resonant state is lost by the nm-order gaps between nanorods.

The strong contrast of *T* in Fig. 5(a) indicates that the 2D nanorod arrays serves as a good polarizer of subwavelength thickness, which is employed in section 4.3.

Dimers or aggregations of rectangular and circular metallic nanostructures have attracted great interest in terms of so-called gap plasmons in terms of enhanced Raman scattering (Futamata et al., 2003; Kneipp, 2007). *T* spectra in Fig. 5 suggest that gap plasmons rapidly disappear as the gap increases and are lost even with a small gap of 10 nm.

In Fig. 5, we show the results on rectangular Ag nanorod array; similar spectral examinations were conducted for circular Ag nanorod arrays though the spectra are not shown here. The qualitative tendency is similar and the contrast of *T* is rapidly lost as the gaps between the circular nanorods increases in nm order.

In Fig. 6, we show *T* spectra of Ag nanorod arrays embedded in a Si layer of 340 nm height along the *z* axis. Incident polarizations were ψ = 45° and 135°. *T* spectra at ψ = 45° and 135° are shown with blue solid and blue dashed lines, respectively. It is first to be noted that *T* spectra at ψ = 135° are almost independent of the gaps between Ag nanorods; *T*'s at the wavelength range more than 1000 nm are several tens of % and exhibit Fabry-Perot-like oscillations coming from the finite thickness of the periodic structure, suggesting that the 2D structure for ψ = 135° is transparent due to off resonance. In contrast, *T* spectra at ψ = 45° vary the shape significantly with changing the gaps and are very sensitive to the gaps. At the 0 nm gap in Fig. 6(a), contrast of *T* is observed at the wavelength range longer than 1500 nm, indicating that the 2D structure in Fig. 4(b) also works as an efficient polarizer. The states at 1770 nm (arrow in Fig. 6(a)) are examined by electric field distributions in Fig. 7.

4.2 Electromagnetic-field distributions on resonances

In Fig. 7, electric-field distributions are shown which correspond to the 2D periodic structure of the unit cell in Fig. 6(a). Incident wavelength is 1770 nm; the wavelength is indicated by an arrow in Fig. 6(a). Colour plots denote intensity of electric field $|\mathbf{E}|$ and arrows stand for 3D electric-field vector. The unit domain used in the computations by the finite element method is displayed. Periodic boundary conditions are assigned to the *xz* and *yz* boundaries.

Figures 7(a) and 7(b) present the electric-field distributions at incident azimuth angle ψ = 45° and 135°, respectively. Incident plane wave travels from the left *xy* port to the right *xy* port. The phase of incident wave at the input *xy* port was defined by $\mathbf{E}_{in}$ = -(sin(45°), cos(45°), 0) in Fig. 7(a) and by $\mathbf{E}_{in}$ = (sin(135°), cos(135°), 0) in Fig. 7(b). The left panels show 3D view and the right panels shows the *xy* section indicated by cones in the left panels.

Electric-field distributions at ψ = 45° in Fig. 7(a) are prominently enhanced at the vicinity of the connecting points of Ag nanorods. The enhanced fields are mostly induced outside the Ag nanorods and oscillate in-phase (or coherently), suggesting that the resonant states are not Mie type. On the other hand, electric-field distributions at ψ = 135° in Fig. 7(b) have local hot spots at the corners of the Ag nanorods. It is usually observed at off resonant conditions. The electromagnetic wave propagates dominantly in the Si part.

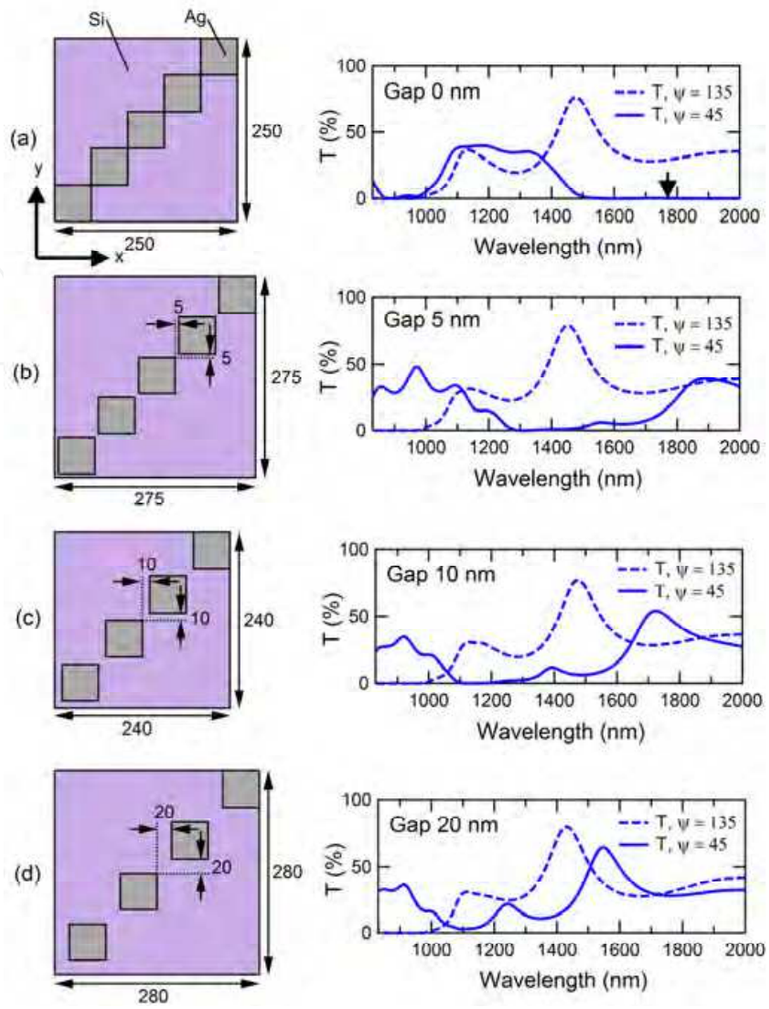


Fig. 6. Unit cell structures and the *T* spectra of Ag nanorod array embedded in a Si layer on SiO_2 substrate. Gaps of Ag nanorods along the *x* and *y* axes are (a) 0 nm, (b) 5 nm, (c) 10 nm, and (d) 20 nm, respectively. Unit cells were set similarly to Fig. 5. *T* spectra at ψ = 45° and 135° are shown with solid and dashed lines, respectively.

Incident power was set to be 2.56×10^2 W/m^2 at the input *xy* port and the corresponding electric-field intensity was 4.39×10^2 V/m. The resonant electric field at the vicinity of nanorod array reaches 4.6×10^3 V/m at the maximum and shows about tenfold enhancement; the scale bar has the maximum of 8.2×10^2 V/m and the distributions are displayed in a saturated way to clearly present them near the connecting points. In air, incident and reflected waves are superimposed in phase and consequently the electric-field intensity takes larger values than the incident power.

4.3 Application for subwavelength circular dichroic devices

As shown in section 4.1, 2D periodic metallic nanorod arrays can serve as polarizers of subwavelength thickness. In this section, we make use of such an efficient polarizer and introduce subwavelength optical devices of circular dichroism.

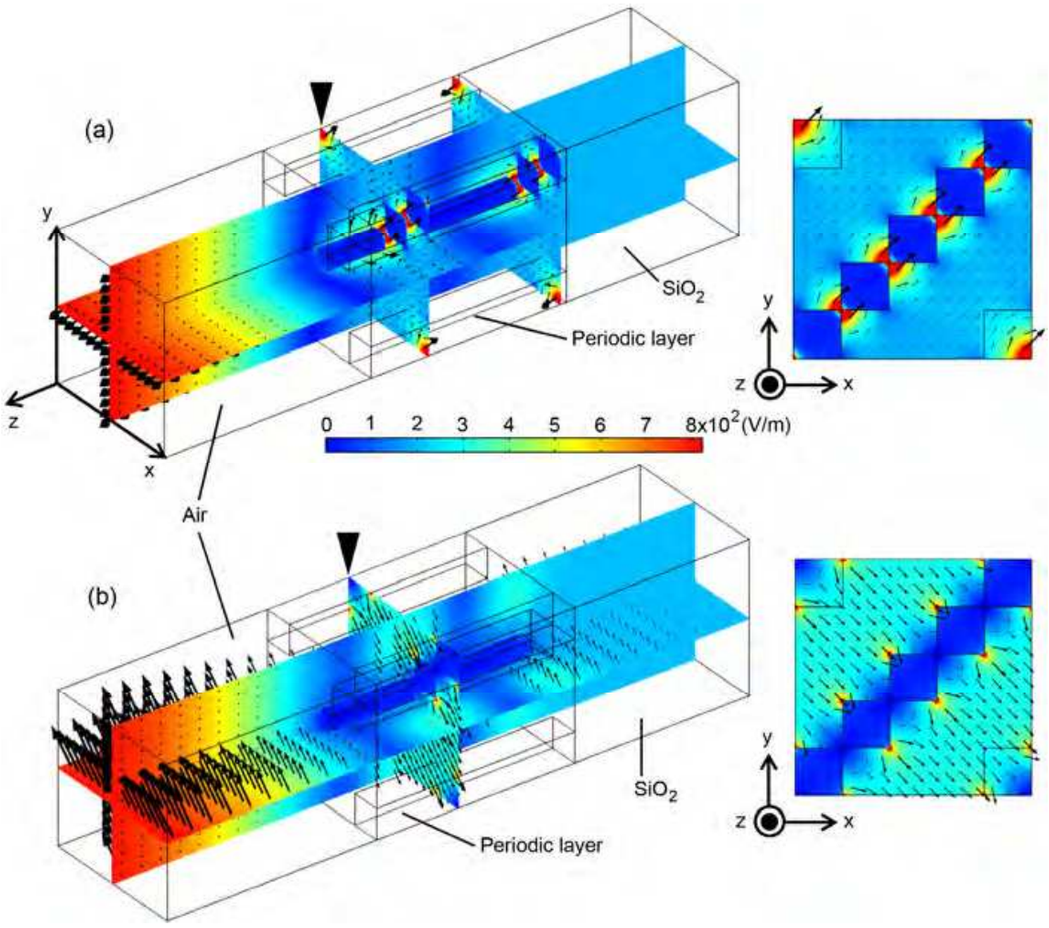


Fig. 7. Electric field distributions of the 2D periodic structure of the unit cell of Fig. 6(a): (a) 1770 nm and ψ = 45°; (b) 1770 nm and ψ = 135°. Left: 3D views of the unit domain. Right: the *xy* sections, indicated by cones in the left panels.

Efficient polarizers selecting polarization vectors are one of the key elements to realize various subwavelength optical devices. Another key element is wave plates which manipulate the phase of electromagnetic waves. In Fig. 8(a), a concrete design of wave plate of subwavelength thickness is presented, which is multilayer structure composed of Ag and SiO_2 and made thin along the layers. Thickness of each Ag and SiO_2 layer along the *x* axis is assumed to be 30 and 270 nm, respectively. Incident light sheds on the side or the *xy* plane. Azimuth angle ψ is defined similarly to Fig. 5(a).

To clarify the basic optical properties of the multilayer structure, *R* spectra at ψ = 0° and 90° under normal incidence are shown in Fig. 8(b). For simplicity, the thickness is assumed to be sufficiently thick to eliminate interference pattern in *R* spectra. For ψ = 0° (that is, $\mathbf{E}_{in}$ is parallel to the x axis), the structure shows small *R* (red dashed line) and is transparent. For ψ = 90° (that is, $\mathbf{E}_{in}$ is parallel to the y axis), it shows *R* spectrum (red solid line) just as a typical Drude metal (Ashcroft & Mermin, 1976). At longer wavelength range than 1000 nm, the structure serves as wire-grid polarizer whereas, at shorter wavelength range than 1000 nm, the structure becomes transparent for any polarization and can work as an efficient wave plate (Iwanaga, 2008).

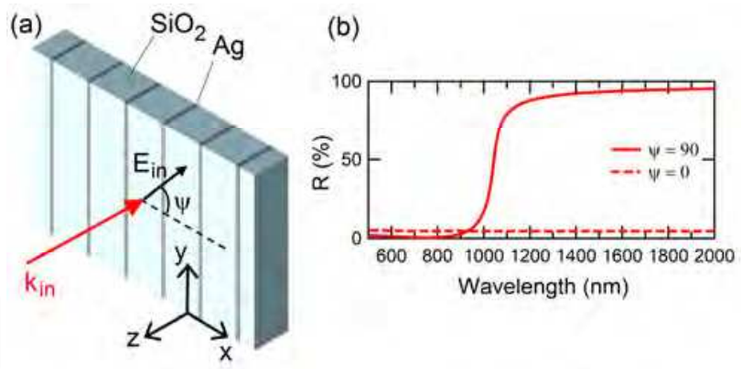


Fig. 8. Wave plate of subwavelength thickness. (a) Schematic drawing of structure and optical configuration. (b) Reflectance spectra under normal incidence at ψ = 0° (dashed line) and ψ = 90° (solid line).

The strong anisotropy of the multilayer structure is quantitatively expressed by using effective refractive index (Iwanaga, 2007a); it was found that, as a wave plate, the *x* axis is fast axis of effective refractive index of about 2 and the *y* axis is very slow axis of effective refractive index less than 1. It is to be emphasized that such strong anisotropy has not been found in solid material and makes it possible for the wave plates of multilayer structure to be extremely thin. In artificial structures, working wavelength can be tuned at desired wavelength by structural modifications; in contrast, it is very hard to change the working wavelength in solid materials because resonance is intrinsic property of materials. The feasibility in tuning is another advantage in subwavelength artificial structures.

Once key elements are found, the combinations are naturally derived and usually realized by producing stacked structures. A recent example is orthogonal polarization rotator of subwavelength thickness, which was numerically substantiated by designing a skew stacked structure of wave plates (Iwanaga, 2010a). By introducing stacked structures, potentials of subwavelength optical devices are greatly extended.

Figure 9(a) shows a concrete design of circular dichroic device (named I), which transforms incident circular polarization to transmitted linear polarization. The circular dichroic device has stacked structure of a wave plate of multilayer structure and a polarizer of 2D Ag nanorod array. The wave plate basically plays a role as a quarter wave plate at the wavelength range of the present interest. Each unit cell of the stacked layers is drawn in detail at the bottom; the dimensions are written in units of nm. Grey denotes Ag and pale blue SiO_2. The thickness of the wave plate and the polarizer was set to be 284 and 210 nm, respectively; therefore, the total thickness of the circular dichroic device was 494 nm.

In Fig. 9(b), *T* spectra under right-handed circular (RHC) and left-handed circular (LHC) polarizations are shown with blue solid and blue dashed lines, respectively. Obviously, definite contrast of *T* appears at about 850 nm. The degree of circular dichroism σ is defined by the following equation.

$$\sigma = \frac{T_{\mathrm{RHC}} - T_{\mathrm{LHC}}}{T_{\mathrm{RHC}} + T_{\mathrm{LHC}}} \tag{3}$$

When σ = 1, the optical device is optimized for RHC and when σ = -1, it is done for LHC. In Fig. 9(c), the σ is shown and takes the value almost equal to unity at 855 nm, which is indicated by a red arrow in Fig. 9(b). Since the thickness of the device is 494 nm, it is confirmed that the circular dichroic device I is certainly subwavelength thickness, which is 58% length for the working wavelength.

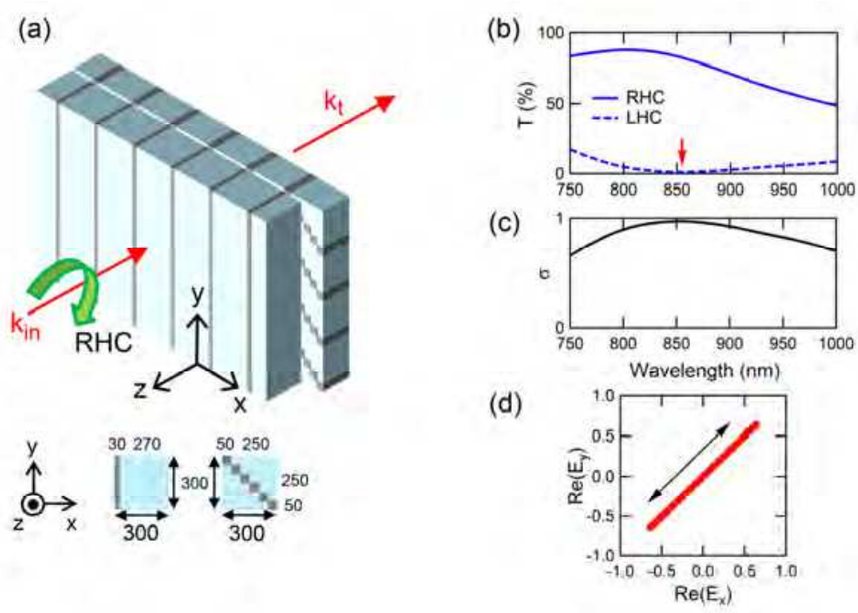


Fig. 9. Circular dichroic device I of subwavelength thickness. (a) Stacked subwavelength structure transforming circular into linear polarizations. (b) Transmittance spectra under RHC (solid line) and LHC (dashed line). (c) Degree of circular polarization σ, defined by equation (3). (d) Polarization of transmitted light.

Figure 9(d) presents polarization of transmitted light (red closed circles). Electric field was recorded for one wavelength and projected onto the *xy* plane. Clearly, the transmitted light is linearly polarized, characterised as ψ = 45° by using azimuth angle ψ.

Figure 10(a) shows schematic drawing of circular dichroic device II, transforming incident circular polarization into counter-circular polarization. The device is composed of stacked structure of wave plate, polarizer, and wave plate and has subwavelength thickness for the working wavelength. Each unit cell of the components is drawn at the bottom and is specified; the first layer means that incident plane waves illuminate first, and succeedingly the incident waves travel through the second and third layers. Grey denotes Ag and pale blue SiO_2. The thickness of the first, second, and third layers is 284, 210, and 255 nm, respectively; the total thickness is 749 nm. Although the basic design of the circular dichroic device I is similar to the device II in Fig. 9, the thickness of the third layer was finely adjusted to obtain ideally circular polarization of transmitted light because evanescent components contribute at the interface of the second and third layers, and modify the electrodynamics in the device II from that at homogeneous interface by plane waves.

Figure 10(b) shows *T* spectra under RHC (blue solid line) and LHC (blue dashed line) incidence. Definite contrast of *T* is observed at 820-900 nm; *T* under LHC incidence is well

suppressed. In Fig. 10(c), the degree of circular dichroism σ is shown, evaluated by equation (3). Almost ideal circular dichroism is realized at 855 nm, indicated by a red arrow in Fig. 10(b).

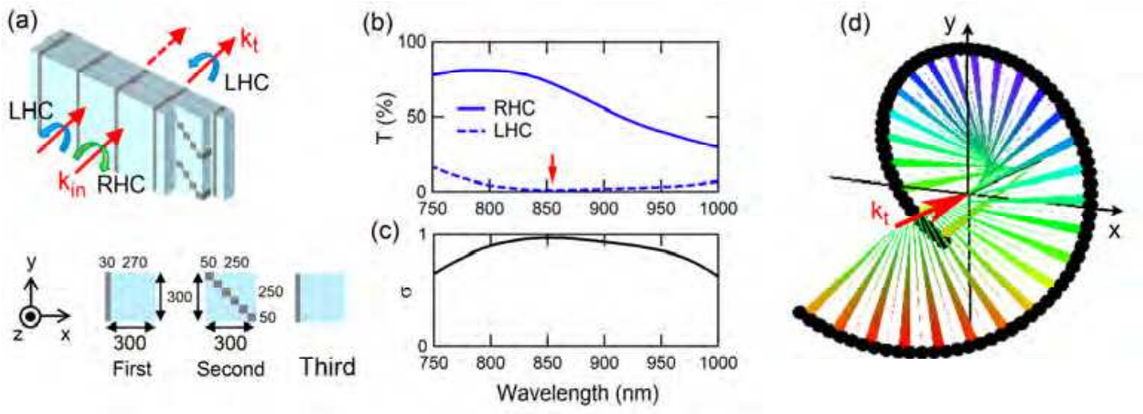


Fig. 10. Circular dichroic device II of subwavelength thickness. (a) Stacked subwavelength structure transforming circular into counter-circular polarizations. (b) Transmittance spectra under RHC (solid line) and LHC (dashed line). (c) Degree of circular polarization σ, defined by equation (3). (d) 3D plot of the trajectory of polarization of transmitted light with wave vector $\mathbf{k}_t$; the wavelength is 855 nm and indicated by an arrow in (b).

Figure 10(d) presents 3D plot of trajectory of the transmitted polarization (or electric field) at 855 nm. The polarization circularly rotates in the left-handed direction along the transmitted wave vector $\mathbf{k}_t$. Thus, it is shown that a unique circular dichroic device transforming incident circular polarization into the counter-circular polarization can be realized with subwavelength thickness by employing metallic nanostructures such as thin line and nanorods. Miniature optical devices shown in this section can serve as key elements in micro-optics circuits in the future.

In considering circular dichroism, it is often preferred to use helical structures. Probably, helical structures are connected unconsciously in mind to helical distributions of polarization such as Fig. 10(d), that is, circular polarizations. In principal, circular dichroism originates from simultaneous manipulations of polarization vector and the phase as proved in Figs. 9 and 10.

Resonances inducing simultaneous change of polarization vector and phase are possibly to be resident in helical structures; an example is periodic array of gold helical structures which serves as a circular dichroic device in infrared range (Gansel et al., 2009). Note that it is impossible to move the working wavelength to the visible range by simply making the smaller structures because scaling law does not hold in the periodic structures including metals which have wavelength-dependent permittivity.

To find new structures serving as circular dichroic devices, nature can provide clues. Jewelled beetles are rather widely known as circular dichroic insects. It turned out that the wings have helically stacked structures (Sharma et al., 2009). Biomimetics thus reminds us to learn from nature.

5. Conclusion

Periodic metallic nanorod arrays have been investigated based on the numerical methods. It was shown that the nanorod arrays have collective resonant states or coherent oscillations outside each nanorod; the field distributions suggest that the resonant states are distinct from Mie resonance. The resonant states form broad band in wavelength, indicating that they are continuum. In the 1D periodic structure of stacked layers, the resonant states are also broad band in incident angles. The doubly broad-band features have not been reported in metallic nanostructures. It was also shown in 2D structures of nanorod array that the structures are crucial to realize the broad-band plasmonic states and that geometrical modifications in the order of 5 nm significantly affect the collective states. Further development of nanofabrications will lead us to the novel plasmonic states. In terms of applications, the 1D nanorod array was discussed as a light managing element for photovoltaic devices and the 2D nanorod arrays were incorporated in highly efficient subwavelength circular-dichroic devices which were concretely designed to work at optical wavelengths, transforming incident circular polarizations to desired polarizations.

6. Acknowledgment

This study was partially supported by Cyberscience Centre, Tohoku University, by JST, PRESTO, and by JSPS KAKENHI (Grant No. 22760047).

7. References

Akahane, Y., Asano, T., Song, B.-S., & Noda, S. (2003). High-Q photonic nanocavity in a two-dimensional photonic crystal. *Nature*, Vol. 425, No. 6961, (October 2003), pp. 944-947, ISSN 0028-0836

Ashcroft, N. W. & Mermin, N. D. (1976). *Solid State Physics* (International ed.), Saunders College Publishing, ISBN 0-03-049346-3, Orlando, United States of America

Bagnall, D. M. &, Boreland, M. (2008). Photovotaic technologies. *Energy Policy*, Vol. 36, No. 12, (December 2008), pp. 4390-4396, ISSN 0301-4215

Born, M. & Wolf, E. (1999). *Principals of Optics* (seventh extended ed.), Cambridge Univ. Press, ISBN 0-521-642221, Cambridge, United Kingdom

Catchpole, K. R. & Polman, A. (2008a). Design principles for particle plasmon enhanced solar cells. *Applied Physics Letters*, Vol. 93, No. 19, (November 2008), pp. 191113-1—191113-3, ISSN 0003-6951

Catchpole, K. R. & Polman, A. (2008b). Plasmonic solar cells. *Optics Express*, Vol. 16, No. 26, (December 2008), pp. 21793-21800, ISSN 1094-4087

Ebbesen, T. W., Lezec, H. J., Ghaemi, H. F., Thio, T., & Wolff, P. A. (1998). Extraordinary optical transmission through sub-wavelength hole arrays. *Nature*, Vol. 391, No. 6668, (February 1998), pp. 667-669

Futamata, M., Maruyama, Y., & Ishikawa, M. (2003). Local Electric Field and Scattering Cross Section of Ag Nanoparticles under Surface Plasmon Resonance by Finite Difference Time Domain Method. *The Journal of Physical Chemistry B*, Vol. 107, No. 31, (August 2003), pp. 7607-7617, ISSN 1520-6106

Gansel, J. K., Thiel, M., Rill, M. S., Decker M., Bade, K., Saile, V., von Freymann, G., Linden, S., & Wegener, M. (2009). Gold Helix Photonic Metamaterial as Broadband Circular

Polarizer. *Science,* Vol. 325, No. 5947, (September 2009), pp. 1513-1515, ISSN 0036-8075

García de Abajo, F. J. (2008). Nonlocal Effects in the Plasmons of Strongly Interacting Nanoparticles, Dimers, and Waveguides. *The Journal of Physical Chemistry C,* Vol. 112, No. 46, (October 2008), pp. 17983-17987, ISSN 1932-7447

Goldberg, D. E. (1989). *Genetic Algorithms in Search, Optimization & Machine Learning*, Addison-Wesley, ISBN 0-201-15767-5, Boston, United States of America

Granet, G. & Guizal, B. (1996). Efficient implementation of the coupled-wave method for metallic lamellar gratings in TM polarization. *Journal of the Optical Society of America A,* Vol. 13, No. 5, (May 1996), pp. 1019-1023, ISSN 0740-3232

Iwanaga, M. (2007a). Effective optical constants in stratified metal-dielectric metamaterial. *Optics Letters,* Vol. 32, No. 10, (May 2007), pp. 1314-1316, ISSN 0146-9592

Iwanaga, M., Vengurlekar, A. S., Hatano, T., & Ishihara, T. (2007b). Reciprocal transmittances and reflectances: An elementary proof. *American Journal of Physics,* Vol. 75, No. 10, (October 2007), pp. 899-902, ISSN 0002-9505

Iwanaga, M. (2008). Ultracompact waveplates: Approach from metamaterials. *Applied Physics Letters,* Vol. 92, No. 15, (April 2008), pp. 153102-1—153102-3

Iwanaga, M. (2009). Optically deep asymmetric one-dimensional plasmonic crystal slabs: Genetic algorithm approach. *Journal of the Optical Society of America B,* Vol. 26, No. 5, (May 2009), pp. 1111-1118, ISSN 0740-3224

Iwanaga, M. (2010a). Subwavelength orthogonal polarization rotator. *Optics Letters,* Vol. 35, No. 2, (January 2010), pp. 109-111

Iwanaga, M. (2010b). Polarization-selective transmission in stacked two-dimensional complementary plasmonic crystal slabs. *Applied Physics Letters,* Vol. 96, No. 8, (February 2010), pp. 083106-1—083106-3

Iwanaga, M. (2010c). Subwavelength electromagnetic dynamics in stacked complementary plasmonic crystal slabs. *Optics Express,* Vol. 18, No. 15, (July 2010), pp. 15389-15398

Iwanaga, M. (2010d). Electromagnetic eigenmodes in a stacked complementary plasmonic crystal slab. *Physical Review B,* Vol. 82, No. 15, (October 2010), pp. 155402-1—155402-8, ISSN 1098-0121

Jackson, J. D. (1999). *Classical Electrodynamics* (third ed.), Wiley, ISBN 0-471-30932-X, Hoboken, United States of America

Kneipp, K. (2007). Surface-enhanced Raman scattering. *Physics Today,* Vol. 60, No. 11, (November 2007), pp. 40-46, ISSN 0031-9228

Ko, D. Y. K. & Inkson, J. C. (1988). Matrix method for tunneling in heterostructures: Resonant tunneling multilayer systems. *Physical Review B,* Vol. 38, No. 14, (November 1988), pp. 9945-9951

Kubo, W. & Fujikawa, S. (2011) Au Double Nanopollars with Nanogap for Plasmonic Sensor. *Nano Letters*, Vol. 11, No. 1, (January 2011), pp. 8-15, ISSN 1530-6984

Kuwata, H., Tamaru, H., Esumi, K., & Miyano, K. (2003). Resonant light scattering from metal nanoparticles: Practical analysis beyond Rayleigh approximation. *Applied Physics Letters,* Vol. 83, No. 22, (December 2003), pp. 4625-4627

Lalanne, P. & Morris, G. M. (1996). Highly improved convergence of the coupled-wave method for TM polarization. *Journal of the Optical Society of America A,* Vol. 13, No. 4, (April 1996), pp. 779-784

Landau, L. D., Lifshitz, E. M., & Pitaevskii, L. P. (1982). *Electrodynamics of Continuous Media* (second ed. revised and extended), Elsevier, ISBN 0-7506-2634-8, Oxford, United Kingdom

Li, L. (1996a). Formulation and comparison of two recursive matrix algorithm for modelling layered diffraction gratings. *Journal of the Optical Society of America A,* Vol. 13, No. 5, (May 1996), pp. 1024-1035

Li, L. (1996b). Use of Fourier series in the analysis of discontinuous periodic structures. *Journal of the Optical Society of America A,* Vol. 13, No. 9, (September 1996), pp. 1870-1876

Li, L. (1997). New formulation of the Fourier modal method for cross surface-relief gratings. *Journal of the Optical Society of America A,* Vol. 14, No. 10, (October 1997), pp. 2758-2767

Liu, N., Guo, H., Fu, L., Kaiser, S., Schwerizer, H., & Giessen, H. (2007). Plasmon Hybridization in Stacked Cut-Wire Metamaterials. *Advanced Materials*, Vol. 19, No. 21, (November 2007), pp. 3628-3632, ISSN 1521-4095

Liu, N., Liu, H., Zhu, S., & Giessen, H. (2009). Stereometamaterials. *Nature Photonics*, Vol. 3, No. 3, (March 2009), pp. 157-162, ISSN 1749-4885

Markoš, P. & Soukoulis, C. M. (2008). *Wave Propagation from Electrons to Photonic Crystals and Left-handed Materials* (first ed.), Princeton Univ. Press, ISBN 978-0-691-13003-3, New Jersey, United States of America

Maxwell-Garnett, J. C. (1904). Colours in Metal Glasses in Metallic Films. *Philosophical Transactions of the Royal Society of London, Series A*, Vol. 203, pp. 385-420, ISSN 0080-4614

Maxwell-Garnett, J. C. (1906). Colours in Metal Glasses in Metallic Films, and in Metallic Solutions. *Philosophical Transactions of the Royal Society of London, Series A*, Vol. 393, pp. 237-288

McMahon, J. M., Gray, S. K., & Schatz, G. C. (2010). Optical Properties of Nanowire Dimers with a Spatially Nonlocal Dielectric Function. *Nano Letters,* Vol. 19, No. 22, (November 2007), pp. 3473-3481

Murray, A., & Barnes, W. L. (2007). Plasmonic Materials. *Advanced Materials,* Vol. 19, No. 22, (November 2007), pp. 3771-3782

Palik, E. D. (1991). *Handbook of Optical Constants of Solids II,* Academic Press, ISBN 978-0-125-44422-4, San Diego, United States of America

Pendry, J. B. & Smith, D. R. (2004). Reversing Light With Negative Refraction. *Physics Today*, Vol. 57, No. 6, (June 2004), pp. 37-43

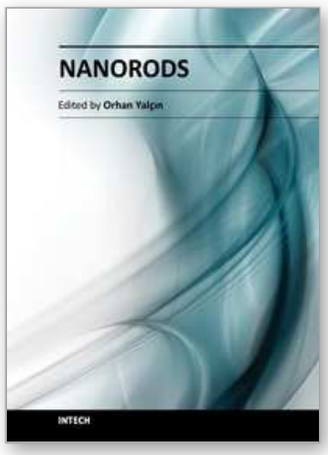
Potten, R. J. (2004). Reciprocity in optics. *Reports on Progress in Physics*, Vol. 67, No. 5, (May 2004), pp. 717-754, ISSN 0034-4885

Prodan, E., Radloff, C., Halas, N. J., & Nordlander, P. (2003). A Hybridazation Model for the Plasmon Response of Complex Nanostructures. *Science*, Vol. 302, No. 5644, (October 2003), pp. 419-422

Raether, H. (1998). *Surface Plasmons on Smooth and Rough Surfaces and Gratings,* Springer, ISBN 0387173633, Berlin, Germany

Rakić, A. D., Djurišić, A. B., Elazar, J. M., & Majewski, M. L. (1998). Optical properties of metallic films for vertical-cavity optoelectronic devices. *Applied Optics,* Vol. 37, No. 22, (August 1998), pp. 5271-5283, ISSN 0003-6935

Sharma, V., Crne, M., Park, J. O., & Srinivasarao, M. (2009). Structural Origin of Circular Polarized Iridescence in Jewelled Beetles. *Science*, Vol. 325, No. 5939, (July 2009), pp. 449-451



Nanorods

Edited by Dr. Orhan Yalçın

ISBN 978-953-51-0209-0

Hard cover, 250 pages

Publisher InTech

Published online 09, March, 2012

Published in print edition March, 2012

The book "Nanorods" is an overview of the fundamentals and applications of nanosciences and nanotechnologies. The methods described in this book are very powerful and have practical applications in the subjects of nanorods. The potential applications of nanorods are very attractive for bio-sensor, magneto-electronic, plasmonic state, nano-transistor, data storage media, etc. This book is of interest to both fundamental research such as the one conducted in Physics, Chemistry, Biology, Material Science, Medicine etc., and also to practicing scientists, students, researchers in applied material sciences and engineers.

How to reference

In order to correctly reference this scholarly work, feel free to copy and paste the following:

Masanobu Iwanaga (2012). Collective Plasmonic States Emerged in Metallic Nanorod Array and Their Application, Nanorods, Dr. Orhan Yalçın (Ed.), ISBN: 978-953-51-0209-0, InTech, Available from: http://www.intechopen.com/books/nanorods/collective-plasmonic-states-emerged-in-metallic-nanorod-array-and-their-application

INTECH
open science | open minds

InTech Europe

University Campus STeP Ri
Slavka Krautzeka 83/A
51000 Rijeka, Croatia
Phone: +385 (51) 770 447
Fax: +385 (51) 686 166
www.intechopen.com

InTech China

Unit 405, Office Block, Hotel Equatorial Shanghai
No.65, Yan An Road (West), Shanghai, 200040, China
中国上海市延安西路65号上海国际贵都大饭店办公楼405单元
Phone: +86-21-62489820
Fax: +86-21-62489821

© 2012 The Author(s). Licensee IntechOpen. This is an open access article distributed under the terms of the Creative Commons Attribution 3.0 License, which permits unrestricted use, distribution, and reproduction in any medium, provided the original work is properly cited.

IntechOpen

IntechOpen